EUROPEAN ORGANIZATION FOR NUCLEAR RESEARCH

CERN–EP/99–114
18 August 1999

A NEW MEASUREMENT OF DIRECT CP VIOLATION IN TWO PION DECAYS OF THE NEUTRAL KAON

The NA48 Collaboration

Abstract

The NA48 experiment at CERN has performed a new measurement of direct CP violation, based on data taken in 1997 by simultaneously collecting K_L and K_S decays into $\pi^0\pi^0$ and $\pi^+\pi^-$. The result for the CP violating parameter $\mathrm{Re}\,(\varepsilon'/\varepsilon)$ is $(18.5 \pm 4.5(\mathrm{stat}) \pm 5.8(\mathrm{syst})) \times 10^{-4}$.

(Submitted to Physics Letters B)

V. Fanti, A. Lai, D. Marras, L. Musa[1)]
Dipartimento di Fisica dell'Università e Sezione dell'INFN di Cagliari, I-09100 Cagliari, Italy

A.J. Bevan, T.J. Gershon, B. Hay, R.W. Moore,[2)] K.N. Moore,[2)] D.J. Munday, M.D. Needham,[3)] M.A. Parker, S.F. Takach,[4)] T.O. White, S.A. Wotton
Cavendish Laboratory, University of Cambridge, Cambridge, CB3 0HE, UK[5)]

G. Barr, H. Blümer,[6)] G. Bocquet, J. Bremer, A. Ceccucci, J. Cogan,[7)] D. Cundy, N. Doble, W. Funk, L. Gatignon, A. Gianoli,[8)] A. Gonidec, G. Govi, P. Grafström, G. Kesseler, W. Kubischta, A. Lacourt, S. Luitz,[9)] J.P. Matheys, A. Norton, S. Palestini, B. Panzer-Steindel, B. Peyaud,[7)] D. Schinzel, H. Taureg, M. Velasco, O. Vossnack, H. Wahl, G. Wirrer
CERN, CH-1211 Geneva 23, Switzerland

A. Gaponenko, V. Kekelidze, D. Madigojine, A. Mestvirishvili,[10)] Yu. Potrebenikov, G. Tatishvili, A. Tkatchev, A. Zinchenko
Joint Institute for Nuclear Research, Dubna, Russian Federation

L. Bertolotto,[1)] O. Boyle, I.G. Knowles, V.J. Martin, H.L.C. Parsons, K.J. Peach, C. Talamonti[11)]
Department of Physics and Astronomy, University of Edinburgh, JCMB King's Buildings, Mayfield Road, Edinburgh, EH9 3JZ, UK[5)]

M. Contalbrigo, P. Dalpiaz, J. Duclos, A. Formica,[7)] P.L. Frabetti,[12)] M. Martini, F. Petrucci, M. Savrié
Dipartimento di Fisica dell'Università e Sezione dell'INFN di Ferrara, I-44100 Ferrara, Italy

A. Bizzeti,[13)] M. Calvetti, G. Collazuol, G. Graziani, E. Iacopini, M. Lenti, A. Michetti
Dipartimento di Fisica dell'Università e Sezione dell'INFN di Firenze, I-50125 Firenze, Italy

H.G. Becker, P. Buchholz,[14)] D. Coward,[9)] C. Ebersberger, H. Fox, A. Kalter, K. Kleinknecht, U. Koch, L. Köpke, B. Renk, J. Scheidt, J. Schmidt, V. Schönharting, Y. Schué, R. Wilhelm, M. Wittgen
Institut für Physik, Universität Mainz, D-55099 Mainz, Germany[15)]

[1)] Present address: CERN, CH-1211 Geneva 23, Switzerland
[2)] Present address: Physics-Astronomy Building, Michigan State University, East Lansing, MI 48824 USA
[3)] Present address: NIKHEF, PO Box 41882, 1009 DB Amsterdam, The Netherlands
[4)] Present address: Department of Physics, Wayne State University, Detroit, MI 48201, USA
[5)] Funded by the UK Particle Physics and Astronomy Research Council
[6)] Present address: Universität Karlsruhe (TH), Fakultät für Physik, and Forschungszentrum Karlsruhe GmbH, Institut für Kernphysik, D-76128 Karlsruhe
[7)] Present address: DSM/DAPNIA - CEA Saclay, F-91191 Gif-sur-Yvette, France
[8)] Present address: Dipartimento di Fisica dell'Università e Sezione dell'INFN di Ferrara, I-44100 Ferrara, Italy
[9)] Present address: SLAC, Stanford, CA 94309, USA
[10)] Present address: Dipartimento di Fisica dell'Università e Sezione dell'INFN di Perugia, I-06100 Perugia, Italy
[11)] Present address: Dipartimento di Fisiopatologia Clinica dell'Università di Firenze, I-50134 Firenze, Italy
[12)] Permanent address: Dipartimento di Fisica dell'Università e Sezione dell'INFN di Bologna, I-40126 Bologna, Italy
[13)] Also at Dipartimento di Fisica dell'Università di Modena, I-41100 Modena, Italy
[14)] Present address: Institut für Physik, Universität Dortmund. D-44221 Dortmund, Germany

J.C. Chollet, S. Crépé, L. Fayard, L. Iconomidou-Fayard, J. Ocariz,[16] G. Unal, D. Vattolo, I. Wingerter-Seez
Laboratoire de l'Accélérateur Linéaire, IN2P3-CNRS, Université de Paris-Sud, F-91406 Orsay, France[17]

G. Anzivino, F. Bordacchini, P. Cenci, P. Lubrano, A. Nappi, M. Pepe, M. Punturo
Dipartimento di Fisica dell'Università e Sezione dell'INFN di Perugia, I-06100 Perugia, Italy

L. Bertanza, A. Bigi, P. Calafiura,[18] R. Carosi, R. Casali, C. Cerri, M. Cirilli, F. Costantini, R. Fantechi, S. Giudici, B. Gorini,[1] I. Mannelli, V. Marzulli, G. Pierazzini, F. Raffaelli, M. Sozzi
Dipartimento di Fisica dell'Università, Scuola Normale Superiore e Sezione dell'INFN di Pisa, I-56100 Pisa, Italy

J.B. Cheze, M. De Beer, P. Debu, R. Granier de Cassagnac, P. Hristov,[19] E. Mazzucato, S. Schanne, R. Turlay, B. Vallage
DSM/DAPNIA - CEA Saclay, F-91191 Gif-sur-Yvette, France

I. Augustin,[1] M. Bender, M. Holder, M. Ziolkowski
Fachbereich Physik, Universität Siegen, D-57068 Siegen, Germany[20]

R. Arcidiacono, C. Biino, R. Cester, F. Marchetto, E. Menichetti, N. Pastrone
Dipartimento di Fisica Sperimentale dell'Università e Sezione dell'INFN di Torino, I-10125 Torino, Italy

J. Nassalski, E. Rondio, M. Szleper, W. Wislicki, S. Wronka
Soltan Institute for Nuclear Studies, Laboratory for High Energy Physics, PL-00-681 Warsaw, Poland[21]

H. Dibon, G. Fischer, M. Jeitler, M. Markytan, I. Mikulec, G. Neuhofer, M. Pernicka, A. Taurok
Österreichische Akademie der Wissenschaften, Institut für Hochenergiephysik, A-1050 Wien, Austria[22]

[15] Funded by the German Federal Minister for Research and Technology (BMBF) under contract 7MZ18P(4)-TP2
[16] Permanent address: Departamento de Física, Universidad de los Andes, Mérida 5101-A, Venezuela
[17] Funded by Institut National de Physique des Particules et de Physique Nucléaire (IN2P3), France
[18] Present address: E.O. Lawrence Berkeley National Laboratory, Berkeley, CA 94720 USA
[19] Present address: Joint Institute for Nuclear Research, Dubna, Russian Federation
[20] Funded by the German Federal Minister for Research and Technology (BMBF) under contract 056SI74
[21] Supported by the Committee for Scientific Research grant 2P03B07615 and using computing resources of the Interdisciplinary Center for Mathematical and Computational Modelling of the University of Warsaw
[22] Funded by the Austrian Ministery for Traffic and Research under the contract GZ 616.360/2-IV GZ 616.363/2-VIII, Austria and by the Fonds für Wissenschaft und Forschung FWF Nr. P08929-PHY

1 Introduction

CP violation has been observed so far only in the decays of neutral kaons [1]. The main component of the effect [2] occurs in the mixing between K^0 and $\bar{K^0}$ eigenstates. The physical states K_S and K_L deviate from pure CP=$\pm$1 eigenstates, with the mixing described by the parameter ε. On the other hand, direct CP violation can occur in the transition from the neutral kaon eigenstate with CP=-1 to a two–pion final state, which has CP=+1. This can be observed through the interference of the amplitudes of different final state isospin [3] and is described by the parameter ε'. The measured quantity is the double ratio of decay widths:

$$R \;=\; \frac{\Gamma(K_L \to\; \pi^0\pi^0\,)/\,\Gamma(K_S \to\; \pi^0\pi^0\,)}{\Gamma(K_L \to \pi^+\pi^-)/\,\Gamma(K_S \to \pi^+\pi^-)} \simeq 1 - 6 \times \mathrm{Re}\,(\varepsilon'/\varepsilon). \qquad (1)$$

The Standard Model relates CP violation to the existence of three generations of quarks and to the complex phase present in the CKM matrix [4]. Computations based on the Standard Model typically predict $\mathrm{Re}\,(\varepsilon'/\varepsilon)$ in the range 0 to 10×10^{-4} [5]. The first evidence for direct CP violation was published in 1988 [6]. Subsequent measurements $(23.0 \pm 6.5) \times 10^{-4}$ [7] and $(7.4 \pm 5.9) \times 10^{-4}$ [8] have been only marginally consistent with each other; the measurement in [7] shows evidence for direct CP violation while that in [8] is consistent with no effect. The KTeV collaboration has recently measured $(28.0 \pm 4.1) \times 10^{-4}$ [9] using a technique similar to the one used in [8].

In this letter, a new measurement of $\mathrm{Re}\,(\varepsilon'/\varepsilon)$ obtained by the NA48 collaboration at CERN is presented, based on the first data collected with the experiment in 1997. While the ultimate accuracy of the NA48 experiment will be significantly better than that reported in this study, this result is of sufficient precision to help clarify the current experimental situation.

2 Principle of measurement

The measurement of $\mathrm{Re}\,(\varepsilon'/\varepsilon)$ proceeds by counting the number of events in each of the four decay modes and computing the double ratio R. The NA48 experiment is designed in such a way that many systematic uncertainties can be controlled with high accuracy by exploiting cancellations of effects which contribute symmetrically to different components of the double ratio.

Data are collected simultaneously in the four decay channels, minimizing the sensitivity of the measurement to accidental activity and to variations in beam intensity and detection efficiency. K_L and K_S decays are provided by two nearly collinear beams, with similar momentum spectra, converging in the centre of the main detector.

In order to reduce the difference in acceptance due to the large difference in average decay lengths, only K_L decays occurring in the region also populated by K_S decays are used for the measurement of the double ratio. Furthermore, a cancellation of the residual difference is obtained by weighting the K_L events used in the double ratio with a function of the proper lifetime τ, proportional to the expected ratio of K_S and K_L decays at time τ. In this way, the systematic accuracy of the result does not rely on a detailed Monte Carlo simulation of the experiment.

3 Beam and detector

3.1 The kaon beams

The neutral beams [10] are derived from 450 GeV/c protons extracted from the CERN SPS. Due to the different mean decay lengths (λ_L=3.4 km, λ_S=5.9 m at the average

kaon momentum of 110 GeV/c), two separate production targets are used, located 126 m and 6 m upstream of the beginning of the decay region.

For each SPS pulse (2.4 s spill every 14.4 s), 1.1×10^{12} protons hit the K_L production target. A neutral secondary beam, with ± 0.15 mrad divergence is generated at a production angle of 2.4 mrad. Three stages of collimation are used with the final element located just upstream of the beginning of the decay region.

Part of the non-interacting primary protons impinge on a bent silicon mono–crystal [11]. A small fraction of these protons undergo channelling, and are bent to produce a collimated beam of 3×10^7 protons per pulse transported to the K_S production target.

The K_S collimator selects secondary neutral particles at 4.2 mrad production angle, with a divergence of ± 0.375 mrad. The different production angles for the K_L and K_S beams are chosen to minimize the difference in decay momentum spectra. The K_S beam enters the fiducial decay volume 68 mm above the K_L beam. The beams converge with an angle of 0.6 mrad and the axes of the two beams cross at the position of the electromagnetic calorimeter. The total flux of K_L through the fiducial region is $\approx 1.5 \times 10^7$ per spill, and the K_S flux is $\approx 2 \times 10^2$ per spill.

The protons directed to the K_S target are detected by an array of scintillation counters which comprise the tagging detector [12]. This device is used to tag K_S decays. The time of any protons and the time of the event in the main detector are each reconstructed relative to a common free running clock. The presence (absence) of a proton reconstructed in coincidence with the event defines the event as K_S (K_L). The signals are digitized by 960 MHz FADCs. The proton time resolution is 120 ps and the double-pulse separation is 4 ns.

The neutral beam produced at the K_S target traverses an anti–counter (AKS), formed by a set of three scintillation counters preceded by an aligned 3 mm thick iridium crystal which enhances photon conversions (1.8 effective radiation lengths) [13]. This detector is used to veto K_S decays occurring upstream, thus providing an accurate definition of the beginning of the decay region.

The decay region is contained in an evacuated ($< 3 \times 10^{-5}$ mbar) 90 m long tank with a 0.9 mm (0.003 radiation lengths) thick polyimide (Kevlar) composite window at the end. The window extends from an inner diameter of 18.4 cm to an outer diameter of 2.3 m. The neutral beam continues in a 16 cm diameter evacuated tube to a (K_L) beam monitor and the beam dump, both downstream of all the detector elements.

3.2 Main detector

The layout of the main detector is shown in figure 1. Kaons which decay into charged pions are measured by a magnetic spectrometer comprised of four drift chambers [14, 15], and a dipole magnet giving a horizontal transverse momentum kick of 265 MeV/c. The volume between the drift chambers is filled with helium at atmospheric pressure. The drift chambers are each comprised of eight planes of sense wires, two horizontal, two vertical and two along each of the 45° directions. Only horizontal and vertical planes are instrumented in DCH3. The resolution in each projection is 90 μm and the average efficiency is 99.5 % per plane. The geometrical accuracy is better than 0.1 mm/m. The momentum resolution is $\sigma_p/p \simeq 0.5\,\% \oplus 0.009\,\% \times p$ (p in GeV/c), where $\oplus$ means that the contributions should be added in quadrature.

Two plastic scintillator hodoscope planes are placed after the helium tank. They are segmented in horizontal and vertical strips, respectively, with widths varying between 6.5 cm and 10 cm, arranged in 4 quadrants. Fast logic provides a signal for the first level

of the $\pi^+\pi^-$ trigger. This trigger requires the presence of tracks in two opposite quadrants of the hodoscope. The hodoscope data are also used in the analysis to determine the event time of $\pi^+\pi^-$ events for the tagging procedure. The time resolution is $\simeq 200$ ps per track.

A quasi–homogeneous liquid krypton electromagnetic (e.m.) calorimeter with 127 cm (27 radiation lengths) long projective tower readout is used to measure the photons from $\pi^0\pi^0$ events. The electrode structure consists of copper/beryllium ribbons extending between the front and the back of the detector with a ± 48 mrad accordion geometry. The 13212 readout cells each have a cross section of 2×2 cm^2 at the back of the active region. The projective towers point to the average K_S decay position (110 m upstream of the detector) so that the measurement of the photon positions is insensitive to the initial conversion depth. The transverse scale at the back plane of the calorimeter is measured to better than 0.2 mm/m. The initial current induced on the electrodes by the drift of the ionization is measured using pulse shapers with 80 ns FWHM and digitized with 40 MHz FADCs [16]. The energy resolution is $\sigma(E)/E \simeq 0.125/E \oplus 0.032/\sqrt{E} \oplus 0.005$ (E in GeV). The spatial resolution is better than 1.3 mm and the time resolution is better than 300 ps for 20 GeV photons.

The e.m. calorimeter incorporates a detector made of a 4 mm thick plane of scintillating fibres located near the maximum of the shower development. This device provides an independent trigger for $\pi^0\pi^0$ decays, and an additional measurement of the event time.

An iron–scintillator hadron calorimeter, 6.7 nuclear interaction lengths thick, is used to complement the krypton calorimeter to measure the energies of hadrons in the trigger. Three planes of scintillation counters, segmented into 25 cm wide counters, shielded by 80 cm thick iron walls, are used for muon identification to reduce the background from $K_L \to \pi\mu\nu$ ($K_{\mu 3}$) events. Seven counter arrays (indicated as ANTI 1 – ANTI 7 on figure 1), consisting of plastic scintillators and iron converters, surround the vacuum and helium tanks to detect photons which miss the calorimeter. In the present analysis, they are only used to monitor accidental activity.

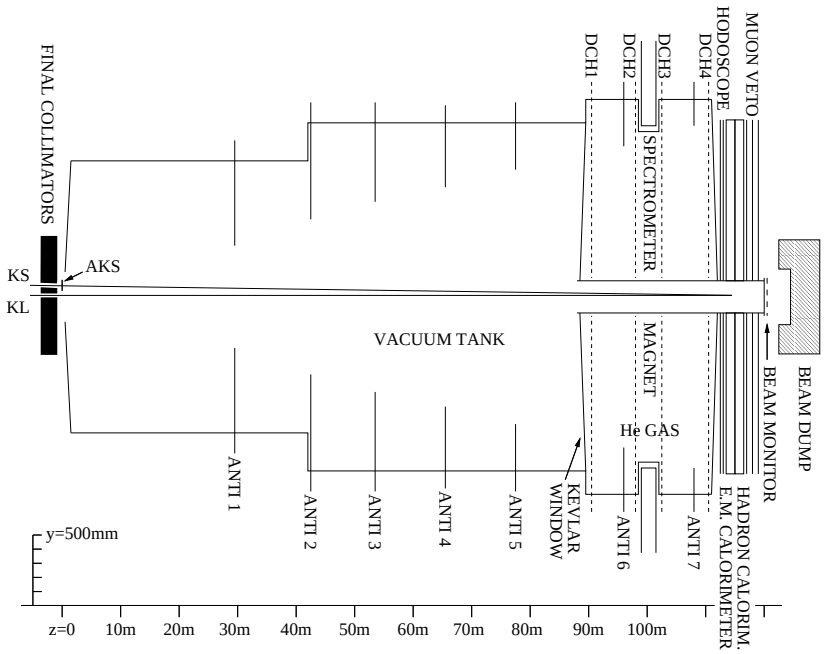

Figure 1: Layout of the main detector components.

3.3 Trigger and DAQ

The readout of the e.m. calorimeter sends the calibrated analogue sums of 2×8 cells to the $\pi^0\pi^0$ trigger. The $\pi^0\pi^0$ trigger [17] digitizes the data and operates as a 40 MHz pipelined computation system with a latency of 3 μs. The calorimeter data are reduced to x and y projections, each consisting of 64 strips, which are used to reconstruct the total deposited energy E_0, the first and second moments of the energy distribution and to reconstruct and measure the time of energy peaks. This information is used to reconstruct the radial position of the centre of gravity C of the event and the proper decay time τ/τ_S in units of the mean K_S lifetime τ_S. Events are selected if $E_0 > 50$ GeV, $C < 15$ cm, $\tau/\tau_S < 5.5$ and if there are no more than five peaks in both views in a 9 ns time window. The $\pi^0\pi^0$ trigger rate is about 4500 per pulse and the deadtime is negligible.

A two level $\pi^+\pi^-$ trigger is used. At the first level, the hodoscope trigger is placed in coincidence with a total energy condition (≥ 30 GeV), defined by adding the hadron calorimeter energy to E_0 from the $\pi^0\pi^0$ trigger. The first level trigger is downscaled by a factor of two, the resulting trigger rate is about 100,000 per pulse. The second level $\pi^+\pi^-$ trigger [18] uses information from the drift chambers. It consists of hardware coordinate builders for each view and a farm of asynchronous microprocessors which reconstructs tracks. Triggers are selected if the tracks converge to within 5 cm, their opening angle is less than 15 mrad, the reconstructed proper decay time is less than 4.5 τ_S and the reconstructed kaon mass is at least 95 % of the nominal K^0 mass. The maximum decision latency is 100 μs. The second level trigger rate is about 2000 per pulse.

Downscaled triggers, based on relaxed conditions are collected to compute the efficiency of the main triggers. "Random events" record any activity in the detectors 69 μs after a heavily downscaled beam counter signal. The 69 μs delay corresponds to the periodicity of the slow proton extraction (three revolution periods) of the SPS accelerator. These events contain signals which are representative of accidental activity in the detectors.

The overall deadtime of the trigger system is below 1 %, the largest contribution being due to the $\pi^+\pi^-$ trigger. The deadtime condition is recorded and made completely symmetric offline. The detector readout systems provide information on all the activity in the detectors in a readout window of about 250 ns surrounding the trigger time. The readout window for the drift chambers is larger, about 1.2 μs.

4 Event reconstruction and selection

4.1 $\pi^0\pi^0$ mode

Photon showers are found in the calorimeter by looking for maxima in the digitized pulses from individual cells in both space and time and accumulating the energy within a radius of 11 cm. Photon energies are corrected for: energy outside the cluster boundary; energy lost in non-working cells (about 0.4 % of the channels); energy from the other photons in the event; small variations of the energy measurement depending on the impact point within the cell and small space charge effects from the accumulation of positive ions [19] because the calorimeter was operated at half the nominal 3 kV drift voltage in 1997.

$K \to \pi^0\pi^0$ decays are selected by requiring four clusters with energies between 3 GeV and 100 GeV which are in time within ± 5 ns of the average of the four. Fiducial cuts are applied to ensure that photon energies are well measured. These cuts include the removal of photons within 2 cm of a non-working cell and photons within a ± 4 cm wide column due to a failure in a HV connection during the 1997 run. The minimum

distance between photon candidates is required to be greater than 10 cm. To reduce the background from $K_L \to 3\,\pi^0$ decays, events with an additional cluster of energy above 1.5 GeV and within $\pm\,3$ ns of the $\pi^0\pi^0$ candidate are rejected.

The kaon energy is obtained with a resolution of $\sim$ 0.6 % from the sum of the photon energies. The longitudinal position of the decay vertex relative to the front of the calorimeter D is reconstructed from the energies E_i and positions x_i, y_i of the four selected clusters, assuming that their invariant mass is the kaon mass (m_K) as follows:

$$D = \sqrt{\sum_i \sum_{j>i} E_i E_j [(x_i - x_j)^2 + (y_i - y_j)^2]} \,/\, m_K \tag{2}$$

and is used to reconstruct the proper decay time τ. The resolution of D is 50 to 70 cm depending on energy. The invariant masses m_1 and m_2 of the two photon pairs are computed using D and compared to the nominal π^0 mass (m_{π^0}). For this, a χ^2 variable is computed as follows:

$$\chi^2 = \left[\frac{(m_1 + m_2)/2 - m_{\pi^0}}{\sigma_+}\right]^2 + \left[\frac{(m_1 - m_2)/2}{\sigma_-}\right]^2 \tag{3}$$

where $\sigma_\pm$ are the resolutions of $(m_1 \pm m_2)/2$ observed in the data (parameterised as a function of the lowest photon energy). The three-fold choice of photon pairings is made by selecting the combination with the lowest χ^2. Due to the constraint on m_K, $(m_1 \pm m_2)$ are to good approximation uncorrelated. Typical values of σ_+ and σ_- are 0.45 and 1.1 MeV/c^2. To select good $\pi^0\pi^0$ candidates, the best combination is required to have $\chi^2 < 13.5$. This requirement removes about 7 % of $K_S \to \pi^0\pi^0$ events in a pure K_S beam where there is no background. About 70 % of these are due to π^0 Dalitz decays and to photon conversions in the Kevlar window or in the spectrometer volume upstream of the magnet. The remaining part is due to the e.m. calorimeter response, and is dominated by occasional photon–nucleon interactions, which result in a reduction of the observed energy. Both effects are highly symmetric between K_S and K_L, and do not affect the measurement of the double ratio.

The event time as used in the tagging procedure for $\pi^0\pi^0$ events is computed combining eight time estimators from the two most energetic cells of each cluster.

4.2 $\pi^+\pi^-$ mode

Tracks are reconstructed from the hits and drift times in the spectrometer. A vertex is defined at the point of closest approach of two oppositely charged tracks (provided they approach to within 3 cm). The momenta of the tracks are derived using a detailed magnetic field map. The energy of the event is reconstructed using the angle between the tracks before the magnet and the ratio of the track momenta, assuming the two tracks originate from $K \to \pi^+\pi^-$. This avoids systematic uncertainties from the knowledge of the magnetic field in the definition of the fiducial energy cut and lifetime measurement. Small corrections on the tracks are made for the field (integral $\sim 2 \times 10^{-3}$ T m) in the decay region before the spectrometer.

The vertex resolution is typically 50 cm in the longitudinal direction z, and 2 mm in the transverse directions x, y. Since the beams are separated by about 6 cm in the decay region, a clean identification of $K_S \to \pi^+\pi^-$ and $K_L \to \pi^+\pi^-$ decays is possible (this is referred to as "y-vertex tagging" in the following).

A variable $\mathcal{A}$ related to the decay orientation in the kaon rest frame is defined from the two track momenta p_1 and p_2 as $\mathcal{A} = |p_1 - p_2|/(p_1 + p_2)$. Kaon energy dependent cuts $\mathcal{A} < 0.62$ and $\mathcal{A} < 1.08 - 0.0052 \times E_K$ (where E_K is the kaon energy in GeV) are made in order to avoid using events with tracks near the beam hole for which a precise Monte Carlo modelling is required. This cut also entirely removes Λ and $\bar{\Lambda}$ decays which are present in the K_S beam.

To reject background from semileptonic K_L decays, tracks consistent with being either an electron or a muon are rejected. To identify electrons, the ratio E/p of the energy of a matching cluster in the e.m. calorimeter to the track momentum is computed. Both tracks must satisfy $E/p < 0.8$. This requirement reduces the $K_L \to \pi e \nu$ (K_{e3}) background by a factor of 500 while removing about 5 % of the $\pi^+\pi^-$ signal. Tracks are identified as muons if hits are found in time in the muon counters near the extrapolated track impact point. Events with identified muons are rejected. The rejection against $K_{\mu 3}$ background is about 500 with an efficiency for $\pi^+\pi^-$ of 97 % (the loss coming essentially from $\pi^\pm$ decays to $\mu^\pm$).

For good $\pi^+\pi^-$ events, the invariant mass $m_{\pi\pi}$ should be equal to the kaon mass. The invariant mass resolution σ_m is typically 2.5 MeV/c^2. An energy dependent cut at $\pm 3\,\sigma_m$ is applied. A further reduction of background due to semileptonic decays is obtained using a cut based on the kaon transverse momentum. To define a selection which is symmetric between K_S and K_L decays, a variable p_t', defined as the component of the kaon momentum orthogonal to the line joining the production target (identified with y-vertex tagging) and the point where the kaon trajectory crosses the plane of the first drift chamber, is used. The p_t' resolution is independent of the target from which the event originated. To select $\pi^+\pi^-$ candidates, the cut $p_t'^2 < 2 \times 10^{-4}$ GeV$^2/c^2$ is applied. Event losses ($\simeq 8 \times 10^{-4}$) are mainly due to large deviations in the vertex reconstruction which are independent of whether the event is K_L or K_S.

The event time as used in the tagging procedure in the $\pi^+\pi^-$ mode is measured by combining the four times from the two hodoscope planes for each track. The procedure which is applied protects against tails in single time measurements (predominantly due to accidental hits). Events for which this procedure cannot be applied are rejected, removing 2.3×10^{-3} of the $\pi^+\pi^-$ signal.

4.3 Tagging

The event is tagged by classifying it as K_S if there is a proton within a ± 2 ns coincidence window centred on the event time, otherwise the event is classified as K_L as shown in figure 2a,c.

An accidental coincidence between a proton traversing the tagger and a K_L event may cause the event to be wrongly counted as K_S. This probability is measured for $\pi^+\pi^-$ events to be $\alpha_{LS}^{+-} = 0.1119 \pm 0.0003$ using y-vertex tagging. The measurement of the double ratio is sensitive to the difference in this probability between $\pi^0\pi^0$ and $\pi^+\pi^-$ events, which is measured to be $\alpha_{LS}^{00} - \alpha_{LS}^{+-} = (10 \pm 5) \times 10^{-4}$ leading to a correction to R of $(18 \pm 9) \times 10^{-4}$. This is measured by looking at proton coincidences at times which are offset from the actual event. Differences in accidental rate between event time and offset coincidence intervals are checked with $K_L \to \pi^+\pi^-$ events, identified from y-vertex tagging, and with $K_L \to 3\pi^0$ events. The observed difference in effective rate seen by $\pi^0\pi^0$ and $\pi^+\pi^-$ events is compatible with the intensity dependence of the $\pi^+\pi^-$ trigger efficiency.

Inefficiencies in reconstructing a proton or errors in measuring the event time or the

proton time can cause a coincidence to be lost and a true K_S event would be classified as K_L. From the y-vertex tagged $\pi^+\pi^-$ events, the probability for this to happen is $\alpha_{SL}^{+-} = (1.5 \pm 0.1) \times 10^{-4}$ (figure 2b). Detailed studies show that this is dominated by inefficiencies in the tagger which are intrinsically symmetric between $\pi^0\pi^0$ and $\pi^+\pi^-$ decays. A sample of neutral events containing π^0 Dalitz decays and photon conversions is used to compare the time measured using the calorimeter with the time of the tracks measured using the hodoscope (figure 2d). This comparison provides the difference between tagging efficiencies for $\pi^0\pi^0$ and $\pi^+\pi^-$ events, which is found to be zero, with an accuracy of $\pm 1 \times 10^{-4}$, leading to an uncertainty on R of $\pm 6 \times 10^{-4}$. As an independent check, $\pi^0\pi^0$ events containing a Dalitz decay have been used to y-vertex tag $\pi^0\pi^0$ events leading to a direct measurement of $\alpha_{SL}^{00} = (2.3^{+3.0}_{-1.0}) \times 10^{-4}$, in agreement with the method above.

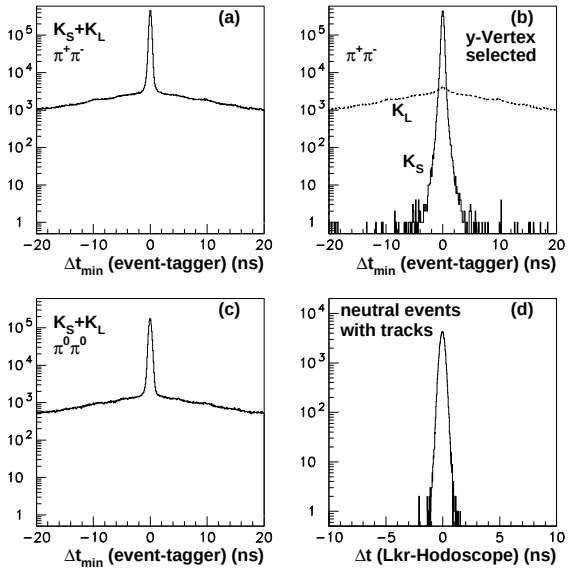

Figure 2: (a) Distribution of the minimum difference between tagger and event times for $\pi^+\pi^-$ decays. The peak corresponds to K_S events where there is a coincidence. (b) The same distribution, separated into K_S and K_L events using y-vertex tagging. This shows that the tails in the coincidence are very small. (c) as (a) for $\pi^0\pi^0$ mode. (d) Coincidence time for neutral events with tracks (see text).

4.4 Data quality selections, data samples

Data collected in the $\pi^+\pi^-$ mode are affected by an overflow condition in the drift chambers which resets the front-end readout buffers when there are more than seven hits in a plane within a 100 ns time interval [15]. This occurs when an accidental particle generates an electromagnetic shower upstream of the spectrometer and sprays the drift chambers with particles. Overflows in each plane are recorded for at least 400 ns before and after each event. To maintain the highest detector efficiency, we require that events used in this analysis do not have overflows within ± 312 ns of the trigger time. This interval, which is larger than the sum of the maximum drift time and reset time, excludes any correlation between overflows and selected events. To avoid indirect biases related to

different average beam intensities, the selection on overflows is also applied to the $\pi^0\pi^0$ mode resulting in a loss of 20 % of the events.

The fiducial range in kaon energy and proper time used to count events is $70 < E_K < 170$ GeV and $0 < \tau < 3.5\ \tau_S$, where $\tau = 0$ is defined at the position of the AKS counter. For K_L, the decay time cut is applied on reconstructed τ, while for K_S the cut at $\tau = 0$ is applied using the AKS to veto events occurring upstream. The nominal $\tau = 0$ position differs by 21.0 ± 0.5 mm between $\pi^0\pi^0$ and $\pi^+\pi^-$ modes, which is accounted for in the analysis. The veto efficiency of the AKS is 0.9964 ± 0.0003 (0.9923 ± 0.0010) for $\pi^0\pi^0$ ($\pi^+\pi^-$) decays and leads to a negligible correction to R.

All events are required to satisfy a symmetric cut on the position of the centre of gravity. For $\pi^0\pi^0$ decays, the centre of gravity is defined as the energy–weighted average x, y position of the four showers at the face of the e.m. calorimeter. For $\pi^+\pi^-$ decays it is the momentum–weighted average position of the track segments, measured upstream of the spectrometer magnet and projected onto the face of the e.m. calorimeter. The radial position of the centre of gravity is required to be within 10 cm of the beam axes. The sensitivity to differences in beam halo and to K_S scattering in the collimator and in the AKS counter is minimized by applying the same cut to both modes. For scattered K_S events, this cut is stronger than the $p_t{}'$ cut applied in the selection of charged events. It is however relatively wide compared to both the K_L and K_S beam–spot radii, which are 3.6 cm and 4.6 cm respectively, so that effects related to resolution smearing can be neglected.

Table 1 shows the number of events collected in each channel after removing background and correcting for mistagged events. The numbers are shown here without lifetime weighting.

Table 1: Statistical samples (in thousands of events).

$K_L \to \pi^0\pi^0$	$K_S \to \pi^0\pi^0$	$K_L \to \pi^+\pi^-$	$K_S \to \pi^+\pi^-$
489	975	1,071	2,087

5 Computation of R and systematic uncertainties

In order to be insensitive to the difference between the beam spectra (about ± 10 % in the range 70–170 GeV), the computation of R is done in 20 energy bins. The numbers of K_S and weighted K_L candidates are corrected for the tagging accidentals and inefficiencies as described above. Corrections for trigger efficiency, background subtraction, and residual acceptance difference between K_S and K_L are applied separately in each energy bin. The average of R over the bins is done with an unbiased estimator of $\log(R)$.

5.1 Trigger efficiency

The efficiency of the $\pi^0\pi^0$ trigger is determined from events triggered by the scintillating fibre detector in the e.m. calorimeter. The average $\pi^0\pi^0$ trigger efficiency is measured to be 0.9988 ± 0.0004 and is the same for K_S and K_L.

The efficiency of the $\pi^+\pi^-$ trigger is measured on a selected sample of events from an auxiliary trigger which reproduces the first level logic. The combined efficiency of the first level coincidence and the second level is 0.9168 ± 0.0009. The major contribution to the inefficiency comes from a timing misalignment in the trigger logic which existed for part of the run. Additional inefficiencies in the hodoscope trigger amount to $(68 \pm 8) \times 10^{-4}$.

The double ratio is corrected by $(+9 \pm 23) \times 10^{-4}$ for the difference between the $\pi^+\pi^-$ trigger efficiency for K_S and τ-weighted K_L decays.

5.2 $\pi^0\pi^0$ background

The background in the $K_L \to \pi^0\pi^0$ sample originates from $K_L \to 3\pi^0$ decays with two undetected photons.

The estimation of the residual background after all cuts is done by extrapolating the number of events in the χ^2 control region 36–135 to the signal region $\chi^2 < 13.5$ as shown in figure 3. The extrapolation factor for the background is measured using a sample of $K_L \to 3\pi^0$ simulated events and is found to be 1.2 ± 0.2 compared to a flat extrapolation (where the error is due to Monte Carlo statistics).

Due to non-Gaussian tails in the χ^2 distribution, the control region contains a mixture of $K_L \to 3\pi^0$ and $\pi^0\pi^0$ events. The number of $\pi^0\pi^0$ events is estimated and subtracted by using the χ^2 distribution shape from tagged K_S events (after correcting for the contamination of accidentally mistagged K_L) and normalising this shape to the K_L χ^2 distribution at small χ^2.

Using this method, the background to the weighted K_L sample is found to be $(8 \pm 2) \times 10^{-4}$ averaged over energy, where the error comes mostly from the Monte Carlo statistical error on the extrapolation factor. Changes in the choice of the control region lead to negligible variations in the estimated background. This procedure is done separately in each energy bin for the R computation, and the background is found to increase from ≈ 0 at 70 GeV to ≈ 0.2 % at 170 GeV.

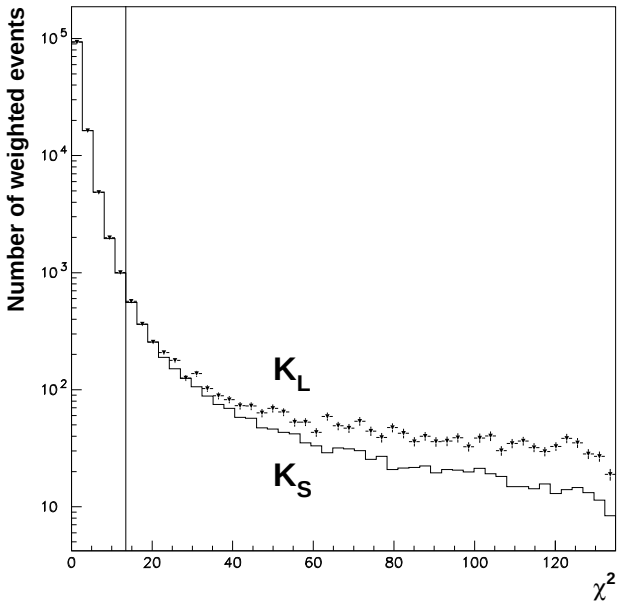

Figure 3: Distribution of χ^2 for weighted K_L candidates (black triangles) compared to the shape for pure $2\pi^0$ events derived from K_S candidates, normalized in the first bin. The excess of events in the K_L candidates in the region $36 < \chi^2 < 135$ is used to extrapolate the background in the signal region ($\chi^2 < 13.5$).

5.3 $\pi^+\pi^-$ background

Semileptonic decays of K_L are selected by identifying the lepton as an electron (from $E/p \simeq 1$) or a muon (from associated hits in the muon counters and low E/p). For each kaon energy bin the event distribution in the $(m_{\pi\pi}, {p_t}'^2)$ plane is determined. The sample of $K_L \to \pi^+\pi^-$ is then fitted as the sum of the contribution from true $\pi^+\pi^-$ decays (determined from the shape of $K_S \to \pi^+\pi^-$), and from the K_{e3} and $K_{\mu 3}$ distributions. Systematic uncertainties are evaluated determining the background in different control regions (contained in the domain $475 \leq m_{\pi\pi} \leq 505$ MeV/c^2 and ${p_t}'^2 \leq 2 \times 10^{-3}$ GeV$^2/c^2$) and verifying the stability of the result for different sub-samples of data. The background in the signal region is $(23 \pm 2(\text{stat}) \pm 4(\text{syst})) \times 10^{-4}$, where the result is averaged over the kaon energy spectrum. The larger contribution is from K_{e3} decays. Figure 4 shows the event distribution in the variable ${p_t}'^2$, for K_L and K_S events, together with the result of the fit to the background.

Kaon decays to $\pi^+\pi^-\gamma$ have been investigated and their effect on R is negligible.

A small fraction ($\simeq 0.5 \times 10^{-3}$) of $K \to \pi^+\pi^-$ are found in the K_L beam at large values of ${p_t}'^2$, extending beyond (3–5) $\times 10^{-3}$ GeV$^2/c^2$. These are due to scattering and regeneration on the collimators. Since these events are removed from the $\pi^+\pi^-$ sample by the ${p_t}'^2$ cut, but satisfy the centre of gravity cut and are kept in the $\pi^0\pi^0$ sample, they cause a correction to the observed value of the double ratio equal to $(-12 \pm 3) \times 10^{-4}$.

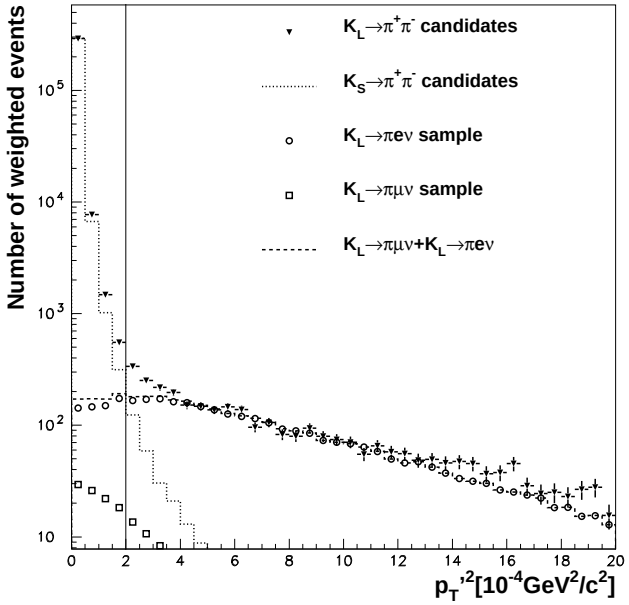

Figure 4: Distribution of ${p_t}'^2$ for K_L candidates fulfilling the $\pi^+\pi^-$ invariant mass cut and result of the fit for the background determination in the control region, including a signal component (derived from K_S events), a K_{e3} component and a $K_{\mu 3}$ component. The final signal region is ${p_t}'^2 < 2 \times 10^{-4}$ GeV^2.

5.4 Energy and distance scale calibrations, stability, linearity

The measurements of the kaon energy, the decay vertex and the proper time in the $\pi^0\pi^0$ mode rely on the measurement of the photon energies and positions in the

calorimeter. The calorimeter performances are studied and adjusted using the $\pi^0\pi^0$ events themselves, K_{e3} decays where the electron energy measured in the calorimeter can be compared to the momentum measured in the spectrometer, and a so-called η run which was a special run with a π^- beam striking a thin target near the AKS counter and producing π^0 and η ($\rightarrow \gamma\gamma$, $3\pi^0$) with known decay position.

The overall energy and distance scale is adjusted using $K_S \rightarrow \pi^0\pi^0$ events. The beginning of the decay region is defined by using the AKS as veto. Therefore the distribution of the reconstructed vertex position exhibits a sharp rising edge at the nominal anti-counter position, as shown in figure 5a. The energy scale is set such that the average value of the reconstructed decay position in a range centred around the anti-counter matches the value found in a Monte Carlo with the nominal scale. This procedure takes into account non-Gaussian tails in the energy resolution. The energy scale was checked daily and was stable within $\pm 5 \times 10^{-4}$ during the entire run. This measurement of the energy scale is checked using the data from the η run. Another check is done using $\pi^0\pi^0$ Dalitz decays and comparing the neutral vertex position with the vertex reconstructed using the charged tracks. The residual uncertainty on the overall energy scale is estimated to be $\pm 5 \times 10^{-4}$ and this leads to an uncertainty of $\pm 5 \times 10^{-4}$ on the double ratio.

The procedure above assumes that the transverse size of the calorimeter is known. The size of the calorimeter is checked using K_{e3} decays, comparing the reconstructed cluster position with the electron track impact point extrapolated to the calorimeter. This comparison is performed with an accuracy of 0.3 mm/m on the transverse scale, which leads to an uncertainty on the double ratio of $\pm 3 \times 10^{-4}$.

The uniformity of the calorimeter response over it's surface is checked and optimised using K_{e3} decays and π^0 decays from the η runs. Residual non-uniformities in the calorimeter response over large distances are at the level of $\approx 10^{-3}$ and the corresponding systematic uncertainty on the double ratio is $\pm 3 \times 10^{-4}$.

The calorimeter energy non-linearity is studied using K_{e3} events, $K_{L,S} \rightarrow \pi^0\pi^0$ events, and π^0 and η decays from the η runs. Non linearities are found to be at the level of 0.3 % in the energy response between 3 and 100 GeV with possible energy offsets of ± 20 MeV. These effects are taken as systematic uncertainties and lead to an uncertainty on the double ratio of $\pm 9 \times 10^{-4}$.

Other uncertainties in the photon energy corrections (energy sharing between clusters and space charge effect), and from residual effects from the difference between the photon direction and the projectivity direction of the calorimeter are estimated to be $\pm 4 \times 10^{-4}$ on the double ratio.

Adding all the previous effects together in quadrature, the total systematic uncertainty coming from the measurement of photon energies and positions is found to be $\pm 12 \times 10^{-4}$ on the double ratio.

For charged decays, the vertex is measured from the reconstructed tracks and is completely determined by the detector geometry. As a check, the anticounter position is fitted on the $K_S \rightarrow \pi^+\pi^-$ events (figure 5b), and agrees to within 1 cm of the expected position. Uncertainties in the geometry and on the residual effect of the magnetic field in the decay region lead to an uncertainty on the double ratio of $\pm 5 \times 10^{-4}$.

5.5 Accidental effects

The effects of accidental activity in the detector are minimized by the simultaneous collection of data in the four channels. Most of the accidental activity is related to K_L decays and to muons originating from the K_L production target.

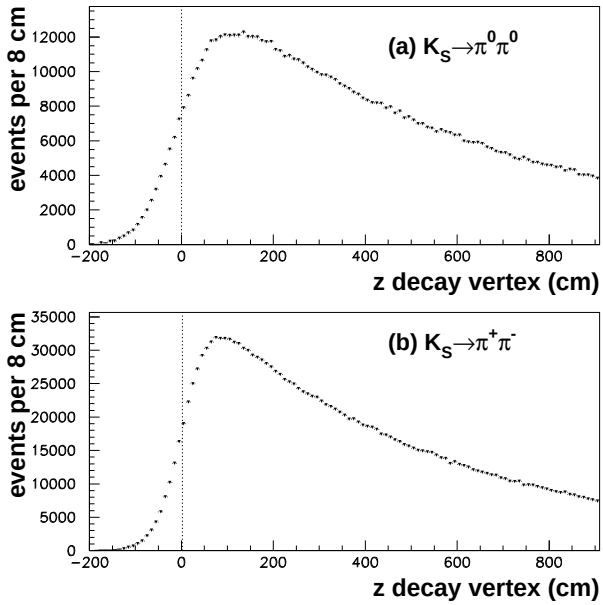

Figure 5: Distribution of the reconstructed decay vertex in K_S events for (a) the $\pi^0\pi^0$ mode and (b) the $\pi^+\pi^-$ mode. The rising edge corresponds to the position of the anticounter (represented by the dotted line).

The accidental rate can be measured directly from the activity in the detector within the readout window before each event. For example, the number of events affected by overflows is the same for $K_L \to \pi^+\pi^-$ and $K_S \to \pi^+\pi^-$ to within the statistical error of 0.1 %. The correction to R due to this particular class of accidentals which prevent the event reconstruction in the drift chambers is negligible after removing events with overflows also from the samples of $\pi^0\pi^0$ decays, as discussed in section 4.4. Other accidentals may however cause a migration of events over the acceptance boundaries. This effect is also expected to be the same for K_S and K_L events due to their kinematical and geometrical similarity.

A method to measure these effects is to overlay events with randomly triggered events which represent accidental activity in the beam, thereby artificially doubling the accidental intensity. The comparison of original and overlaid events provides a direct measurement of intensity effects in terms of gains and losses of events which are at the level of a few percent. As expected the effects tend to cancel in the double ratio. The correction due to accidentals is $(-2 \pm 14) \times 10^{-4}$, where the error is dominated by the statistical uncertainty in the sample of the events used for the overlay analysis.

The overlay technique does not cope with any additional detector activity in the K_S beam generated by the same proton which produced the K_S event. Studies of this background show that the effect on the double ratio can be neglected.

5.6 Acceptance correction

The K_S and K_L acceptances are made very similar in both modes by using the technique of weighting K_L events according to their proper decay time so that the effective longitudinal vertex distribution of K_L events is made equal to the K_S distribution. The weighting factor includes small contributions from interference and K_S decays in the K_L

beam, both of which are significant only for kaon energies above 140 GeV. The residual acceptance differences are studied with a full simulation of the beams and detector. The Monte Carlo sample is five times larger than the event sample. The main sources of systematic error in the acceptance correction are due to uncertainties in the positions and divergences of the beams and a significant component is caused by the dead column in the e.m. calorimeter. The overall $\pi^+\pi^-$ reconstruction efficiency has been found to be the same for K_S and K_L decays using a Monte Carlo computation which includes the measured efficiencies of each drift chamber wire. The acceptance correction is evaluated and applied in each energy bin. The overall correction to the double ratio, averaged over kaon energies in the interval 70—170 GeV is $(29 \pm 11(\mathrm{MCstat}) \pm 6(\mathrm{syst})) \times 10^{-4}$.

6 Result

The effects of the corrections applied to the double ratio are listed in table 2. The systematic errors shown in the first four lines of table 2 are dominated by the statistics of the control sample used in each study and are therefore statistical in nature.

Table 2: Corrections applied to R and systematic uncertainties, in 10^{-4} units.

Tagging $\Delta\alpha_{LS}$, $\Delta\alpha_{SL}$	$+18$	$\pm$	11
$\pi^+\pi^-$ trigger efficiency	$+9$	$\pm$	23
Acceptance	$+29$	$\pm$	12
Accidental effects	-2	$\pm$	14
$\pi^0\pi^0$ background	-8	$\pm$	2
$\pi^+\pi^-$ background	$+23$	$\pm$	4
Scattering/regeneration	-12	$\pm$	3
Energy scale and linearity		$\pm$	12
Charged vertex		$\pm$	5
Total correction	$+57$	$\pm$	35

The values of the double ratio in each bin of kaon energy are shown in figure 6, after trigger efficiency, tagging, background and acceptance corrections are included in each bin. The bins which are used in the analysis, between 70 and 170 GeV (decided prior to running the experiment), are shown with black symbols. The χ^2 of the average is 25.7 (19 d.o.f.). Extensive checks have been made to exclude systematic biases which could lead to a variation of R with the kaon energy as the data might suggest. As a further check, the double ratio R was computed in three additional energy bins, as indicated in figure 6. These three extra points strongly disfavour the hypothesis of a linear trend in the data.

The final result for the double ratio is $R = 0.9889 \pm 0.0027 \pm 0.0035$, where the first error is statistical and the second is systematic. The corresponding value for the direct CP violating parameter is:

$$\mathrm{Re}\,(\varepsilon'/\varepsilon) = (18.5 \pm 4.5 \pm 5.8) \times 10^{-4}$$

Combining the two errors in quadrature, the result is:

$$\mathrm{Re}\,(\varepsilon'/\varepsilon) = (18.5 \pm 7.3) \times 10^{-4}$$

In conclusion, this new measurement of $\mathrm{Re}\,(\varepsilon'/\varepsilon)$ confirms that direct CP violation occurs in neutral kaon decays.

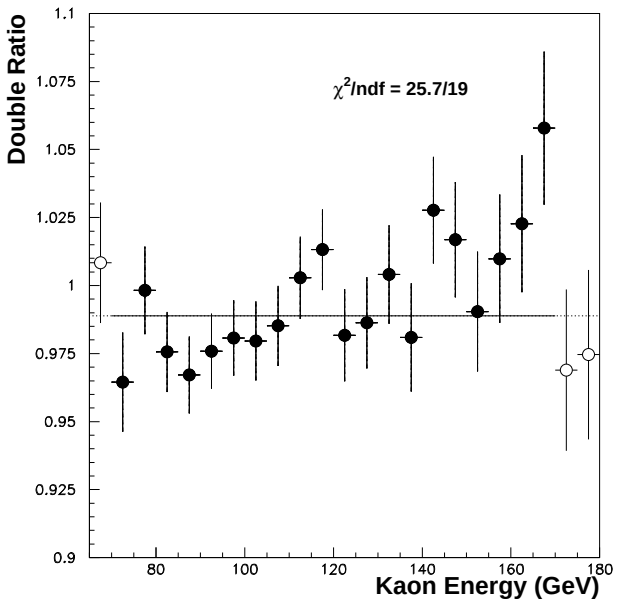

Figure 6: Measured double ratio in energy bins. The points used for the measurement of $\mathrm{Re}\,(\varepsilon'/\varepsilon)$ are shown in black (energy range 70-170 GeV).

Acknowledgements

We would like to warmly thank the technical staff of the participating laboratories and universities for their dedicated effort in the design, construction, and maintenance of the beam, detector, data acquisition and processing.

References

[1] J.H. Christenson, J.W. Cronin, V.L. Fitch, and R. Turlay, Phys. Rev. Lett. 13 (1964), 138.
[2] L. Wolfenstein, Phys. Rev. Lett. 13 (1964) 562.
[3] T.T. Wu and C.N. Yang, Phys. Rev. Lett. 13 (1964) 380.
[4] M. Kobayashi and T. Maskawa, Prog. Theor. Phys. 49 (1973) 652.
[5] A. Buras et al., Phys. Lett. B 389 (1996) 749;
M. Ciuchini et al., Z. Phys. C 68 (1995) 239;
S. Bertolini et al. Nucl. Phys. B 514 (1998) 93;
T. Hambye et al. Phys. Rev. D 58 (1998) 14017.
[6] H. Burkhardt et al., Phys. Lett. B 206 (1988) 169.
[7] G.D. Barr et al., Phys. Lett. B 317 (1993) 233.
[8] L.K. Gibbons et al., Phys. Rev. Lett. 70 (1993) 1203.
[9] A. Alavi-Harati et al., Phys. Rev. Lett. 83 (1999) 22.
[10] C. Biino et al., CERN–SL–98–033 (EA).
[11] N. Doble, L. Gatignon and P. Grafström, Nucl. Instr. and Methods B119 (1996) 181.
[12] P. Grafström et al., Nucl. Instr. and Methods A 344 (1994) 487;
H. Bergauer et al., Nucl. Instr. and Methods A 419 (1998) 623.
[13] R. Moore et al., Nucl. Instr. and Methods B 199 (1996) 149.
[14] D. Bédérède et al., Nucl. Instr. and Methods A 367 (1995) 88.

[15] I. Augustin et al., Nucl. Instr. and Methods A 403 (1998) 472.
[16] B. Hallgren et al., Nucl. Instr. and Methods A 419 (1988) 680;
C. Cerri, Proc. VI Int. Conf. on Calorimetry in HEP, Frascati 1996, A. Antonelli et al. ed., Frascati Physics Serie 6 (1996) 841;
G. Martin-Chassard et al., ibid. 799.
[17] B. Gorini et al., IEEE Trans. Nucl. Sci. 45 (1998) 1771.
[18] S. Anvar et al., Nucl. Instr. and Methods A 419 (1998) 686.
[19] S. Palestini et al., Nucl. Instr. and Methods A 421 (1999) 75.